Supporting Information

SI Text

Relative Speed of Interacting Microcracks as Deduced from the Geo- **metry of Conic-Like Markings.** Fig. S2A depicts the interaction between two microcracks growing radially at velocities c_1 and c_2, respectively. Calling Δ the distance between the two nucleation centers and τ the time interval between the nucleations of the first and second microcracks, the equation describing the successive locations of intersection points (and hence the conic-like marking) is given by

$$\frac{y}{\Delta} = \pm\sqrt{-\left(\frac{x}{\Delta}\right)^2 + \frac{c^2+1}{(c^2-1)^2}\left[c^2\left(\frac{c_1\tau}{\Delta}\right)^2 - \frac{2x}{\Delta}\right] + \frac{1}{(c^2-1)^2} + \frac{2c^2}{(c^2-1)^2}\frac{c_1\tau}{\Delta}\sqrt{\left(1-\frac{2x}{\Delta}\right)(c^2-1) + c^2\left(\frac{c_1\tau}{\Delta}\right)^2}}, \quad \textbf{[S1]}$$

where $c = c_2/c_1$ and (x,y) are expressed in a frame the origin of which is the first nucleation center and the x axis goes through both centers (see Fig. S2A). As can be seen in Fig. S2 B and C, qualitatively different shapes are predicted by this equation depending on the velocity ratio c_2/c_1: true (mathematical) conics when $c_2/c_1 = 1$, egg shapes when $c_2/c_1 < 1$, and flared shapes when $c_2/c_1 > 1$. The fact that the markings observed on the postmortem fracture surfaces look like conics hence suggests a velocity ratio close to unity.

To assess quantitatively the value of the velocity ratio, we directly extracted c_2/c_1 for each pair of interacting microcracks from the marking's geometry on the fractographic images (see Fig. 2B and Fig. S4, *Upper*). Note that seemingly continuous conic-like markings often result from the successive interactions between more than two microcracks, and are hence actually made of several branches, each of them associated with a single pair of interacting microcracks. The analysis procedure we developed is as follows: (*i*) The nucleation centers of two interacting microcracks are selected on the image; (*ii*) the apex of the associated marking is determined as the intersection of the segment relating the two centers and the marking's branch lying in between; (*iii*)

the marking's shape predicted by Eq. **S1** is plotted for various ratio c_2/c_1 while adjusting $c_1\tau/\Delta$ so that the apex position remains fixed; and (*iv*) the value c_2/c_1 that best fits the experimental marking is selected. Typical examples of the cumulative distributions obtained for c_2/c_1 are presented in Fig. 3B and Fig. S4, *Lower*. For all the fractographic images analyzed, the distributions were found to be roughly Gaussian, with mean values around 0.98–0.99 and standard deviation of 0.02–0.03, irrespective of the density ρ of conic-like markings. Note that local stationarity of the average crack front over the millimeter length scales of the analyzed fractographic images should imply a geometric mean value of c_2/c_1 strictly equal to one. The dispersion smallness around one allows identification of this geometric mean with the standard arithmetic one. The observation of a mean value systematically slightly smaller than unity is attributed to an initial accelerating transient in microfracturing events that is not taken into account to derive Eq. **S1**.

It is then justified to assume that all microcracks propagate at the same constant velocity $c_1 = c_2 = c_m$ on a given fractographic image. Eq. **S1** can then be simplified to

$$\frac{y}{\Delta} = \pm\sqrt{4\frac{d_n(2\Delta - d_n)}{(\Delta - 2d_n)^2}\left(\frac{x}{\Delta}\right)^2 - 4\frac{d_n(2\Delta - d_n)}{(\Delta - 2d_n)^2}\left(\frac{x}{\Delta}\right) + \frac{d_n(2\Delta - d_n)}{(\Delta - 2d_n)^2} - 4\left(\frac{d_n}{\Delta}\right) + 4\left(\frac{d_n}{\Delta}\right)^2}, \quad \textbf{[S2]}$$

where $d_n = \Delta - c_m\tau$ is the distance between the triggering front and the nucleation point at the instant of microcrack nucleation and is equal to twice the distance between the marking's apex and focus. Note that, contrary to Eq. **S1**, Eq. **S2** describes a true mathematical conic (see Fig. 2C), the eccentricity and focal parameter of which depend on both d_n and Δ.

Variation of Microcrack Density with Stress Intensity Factor. The K dependency of ρ (Fig. 3A, *Lower*) has been understood in ref. 1 by assuming the material to contain a population of local weak zones, so-called source-sinks (SS). Each one is able to turn into a microcrack provided two conditions are met: (*i*) The local stress at the considered SS reaches a threshold value σ_* (smaller than the local yield stress σ_Y), and (*ii*) the SS is located at a distance from the crack front larger than d_a. Calling ρ_v the SS volume density, the surface density ρ is then equal to the number of activated SS beyond d_a per unit of fracture area (i.e., $\rho_v\{h_\perp - 2d_a - \rho V\}$), where $h_\perp$ is the thickness (size orthogonal to the fracture plane) of the fracture process zone (i.e., the layer in which the stress is larger than σ_*). V is the excluded volume around nucleated microcracks. The universal square root singular form taken by the elastic stress field around the tip of the growing crack gives $h_\perp = K_d^2/\alpha_2\sigma_*^2$ where α_1 is a dimensionless constant close to unity, and K_d relates to K via $K_d = k(c_m)K$ with $k(c_m) = (1 - c_m/c_R)/\sqrt{1 - c_m/c_D} \approx 0.81$ (3). Finally, one gets

$$\rho = C(K^2 - K_a^2) \quad \text{with} \quad C = \frac{\rho_v}{1 + \rho_v V}\frac{k^2(c_m)}{\alpha_1\sigma_*^2} \quad \text{and}$$
$$K_a^2 = \frac{2\alpha_1\sigma_*^2 d_a}{k^2(c_m)}. \quad \textbf{[S3]}$$

The parameter K_a represents then the value of K at the onset of microcracking. Below this value, microcracks cannot nucleate and $\rho = 0$. Eq. **S3** is found to reproduce the experimental data fairly well (see Fig. 3A, *Lower*, in the main text) up to a value $K_b \approx 3.1$ MPa·m$^{1/2}$, which is associated with the microbranching onset (see ref. 1). The loss of agreement above K_b is actually expected because linear elastic fracture mechanics is invalid in the presence of microbranches (see ref. 2). The fitted parameters C and K_a are found to be $C = 9.0 \pm 0.5 \times 10^6$ MPa^{-2}·m^{-3} and $K_a = 2.1 \pm 0.1$ MPa·m$^{1/2}$, respectively.

Variation of Mean Distance at Nucleation with Microcrack Density. In the scenario invoked above, the relation between the mean distance at nucleation $\bar{d}_n$ and K_d is deduced from the universal square root singular form taken by the elastic stress field around the tip of the growing crack (see, e.g., ref. 3). The mean distance $\bar{d}_n$ at which the stress level reaches σ_* then reads $\bar{d}_n = K_d^2/\alpha_2\sigma_*^2$, where α_2 is a dimensionless constant close to unity. This relation together with Eq. **S3** yields

$$\bar{d}_n = \frac{\alpha_1}{\alpha_2}\frac{1+\rho_v V}{\rho_v}\rho + 2\frac{\alpha_1}{\alpha_2}d_a. \qquad \textbf{[S4]}$$

This equation is found to reproduce the experimental data fairly well (see Fig. 3C, *Lower*) up to the point where ρ reaches the value $\rho_{sat} = 45.5$ mm^{-2} defined in Fig. 3A, *Lower* and identified with the microbranching onset. The fitted parameters are found to be $\alpha_1(1+\rho_v V)/\alpha_2\rho_v \approx 10^6$ μm^3 and $2\alpha_1 d_a/\alpha_2 \approx 4.5$ μm.

Saturation of $\bar{d}_n$ and Avalanches. Fig. S6 superimposes the variation of the mean distance at nucleation $\bar{d}_n$ with ρ (presented in Fig. 3C, *Lower*) to the variation of the mean nearest-neighbor distance $\langle\Delta r\rangle$ with ρ. For a Poissonian distribution, $\langle\Delta r\rangle = 1/(2\sqrt{\rho})$, whereas the variance is given by $\sigma^2_{\Delta r} = (4-\pi)/(4\pi\rho)\approx0.068/\rho$. When ρ becomes of the order of ρ_{sat}, the distance between some nucleation centers and the centers of their triggering microcrack becomes smaller than the distance necessary for them to nucleate. Hence, both centers will open almost simultaneously (within the same time step), and an avalanche will occur. This steric effect yields an effective mean distance at nucleation $\bar{d}_n$ (as measured from fracture surfaces) that saturates above ρ_{sat} at a value $\bar{d}_n \approx 50$ μm. The proportion of microcracks involved in nucleation avalanches increases significantly in the vicinity of ρ_{sat} (solid squares in Fig. S6). However, this proportion remains small, less than 7% over the explored range of densities, which explains why the mean-field model yielding Eq. **1** captures so well the increase of the acceleration factor with ρ, even above ρ_{sat} (see Fig. 5B).

Edge Effects in the Deterministic Reconstruction. Once the growth rule $c_2 = c_1$ has been ascertained experimentally, and once the nucleation center location and distance at nucleation of all individual microcracks have been determined from image analysis, the main source of mismatch between the reconstruction and the actual fracture surfaces are errors in the time succession of nucleation events. Such errors are unavoidable when using partial images (a few square millimeters) of the complete fracture surface (a few square centimeters). Along the top and bottom sides of the image, we lack for the possibility of being triggered by microcracks outside the field of view. From the left side of the image, we lack for a realistic initial front shape which would contain all the information about the precise instants at which the leftmost centers have to be nucleated during the reconstruction. Because no information could be obtained about this initial front shape, we arbitrarily chose a straight vertical front as an initial condition.

In Fig. S7, we illustrate the degree of sensitivity of the reconstruction results to changes in the initial front shape, by running the simulation with a sinusoidal initial front. Its period is chosen to roughly match the average vertical distance between simultaneously propagating microcracks. Its amplitude is set to the mean value of the standard deviation of the horizontal location of the total front as obtained using an initial straight front. The same sinusoidal shape, but translated vertically by half a period, was

also tested. As the front involves more generations of microcracks, the patterns become more alike, and hence less affected by the initial conditions. However, some differences can propagate over the whole image. We emphasize that nearly perfect reconstructions could have been obtained through the analysis of images showing the region where the first microcracks nucleate, because it would have allowed for the determination of the actual initial front shape.

The crucial point for our study is to check that the reconstruction errors induced by edge effects do not quantitatively affect the value A of the acceleration factor. Fig. S7 shows that, for the three very different initial front shapes tested, A is found constant within less than 0.6%. This check demonstrates that the average velocity measurement hardly depends on edge effects. These results were found to be robust to changes in period and amplitude of the sinusoidal initial front.

Lattice Model. The variations of the ratio between the macro- and microscale velocities (i.e., the acceleration factor A) as a function of microcrack density ρ can be captured by a simple mean-field model. In the model, the nucleation centers are placed at the nodes of a square lattice, so that the distance ℓ between two neighboring centers is kept constant and equal to $\ell = 1/\sqrt{\rho}$. This model arrangement is depicted in Fig. S8, where x and z axes are chosen parallel to mean crack propagation direction and to mean crack front, respectively. At $t = 0$, the leftmost nucleation centers are turned into microcracks and start to grow radially at velocity c_m. The fronts then trigger the nucleation of the next centers when the shortest distance between the nucleation centers and the fronts reaches a distance of $\bar{d}_n$. The nucleated microcracks then grow radially, coalescing with each other and with the primary crack. The new microcracks trigger the nucleation of the next microcracks, and so on. Because of the invariance to translation along the z axis, the crack can be considered to propagate in the x direction only (see Fig. S8). When the main front has traveled over a distance $L = Ac_m t$ along this line, it has triggered $L/\ell = L\sqrt{\rho}$ microcracks. And because each coalescence with a microcrack makes the rightmost point jump over a distance $\bar{d}_n$, while the crack velocity is c_m between these coalescence events, one also gets $L = c_m t + L\bar{d}_n\sqrt{\rho}$. From the two expressions for L, it can be deduced that $A = 1/(1 - d_n\sqrt{\rho})$.

In real materials, the centers are not aligned along lines parallel to the direction of mean crack propagation but are distributed randomly. We thus propose to modify this equation into

$$A = \frac{1}{1 - b\bar{d}_n\sqrt{\rho}}, \qquad \textbf{[S5]}$$

where the geometrical constant b (expected to be close to one) accounts for the projection onto the x axis of (*i*) the real distance between successive nucleation centers and (*ii*) the distance jumped during a coalescence event with a nonaligned microcrack. This equation is the one proposed in the main text (Eq. **1**).

1. Scheibert J, Guerra C, Célarié F, Dalmas D, Bonamy D (2010) Brittle-quasibrittle transition in dynamic fracture: An energetic signature. *Phys Rev Lett* 104:045501.
2. Sharon E, Fineberg J (1999) Confirming the continuum theory of dynamic brittle fracture for fast cracks. *Nature* 397:333–335.

3. Freund LB (1990) *Dynamic Fracture Mechanics* (Cambridge Univ Press, Cambridge, England), pp 296–366.
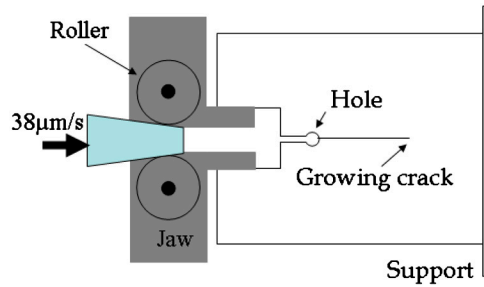
Fig. S1. Sketch of the so-called wedge splitting geometry used to grow dynamic cracks in polymethylmethacrylate (see *Materials and Methods* and ref. 1).
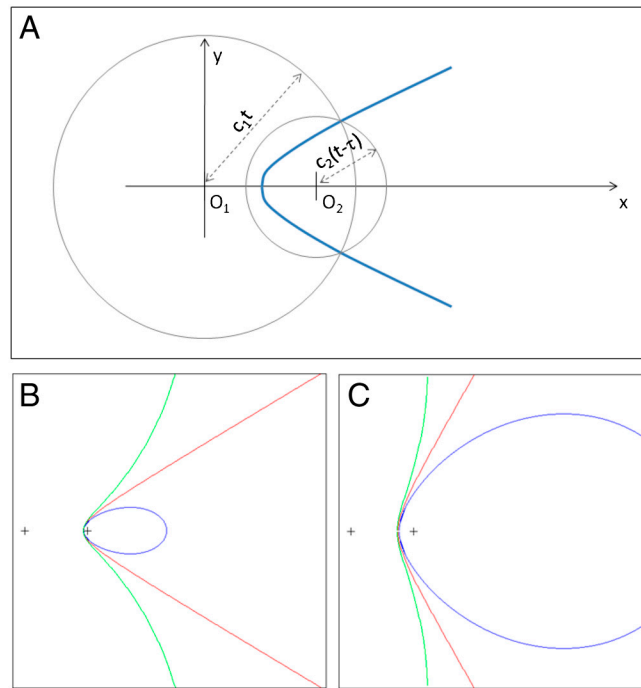

Fig. S2. Geometry of conic markings. (*A*) Sketch underlying Eq. **S1**. A first microcrack nucleates at time $t = 0$ at frame origin O_1 and subsequently grows at velocity c_1. A second microcrack nucleates at time τ at point O_2 of coordinates ($x = \Delta$, $y = 0$) and subsequently grows at velocity c_2. The two gray circles correspond to both microcrack fronts at time t, if microcrack interaction was ignored. In reality, the intersection of the two fronts leaves on the fracture surface a marking that develops as the blue curve as time t increases. In dimensionless coordinates x/Δ and y/Δ, the marking aspect is set by the ratios c_2/c_1 and $c_1\tau/\Delta$. The forms obtained for $c_2/c_1 = 0.9$ (blue), $c_2/c_1 = 1$ (red), and $c_2/c_1 = 1.1$ (green) are plotted in *B* and *C*, for $c_1\tau/\Delta = 0.05$ and $c_1\tau/\Delta = 0.2$, respectively.
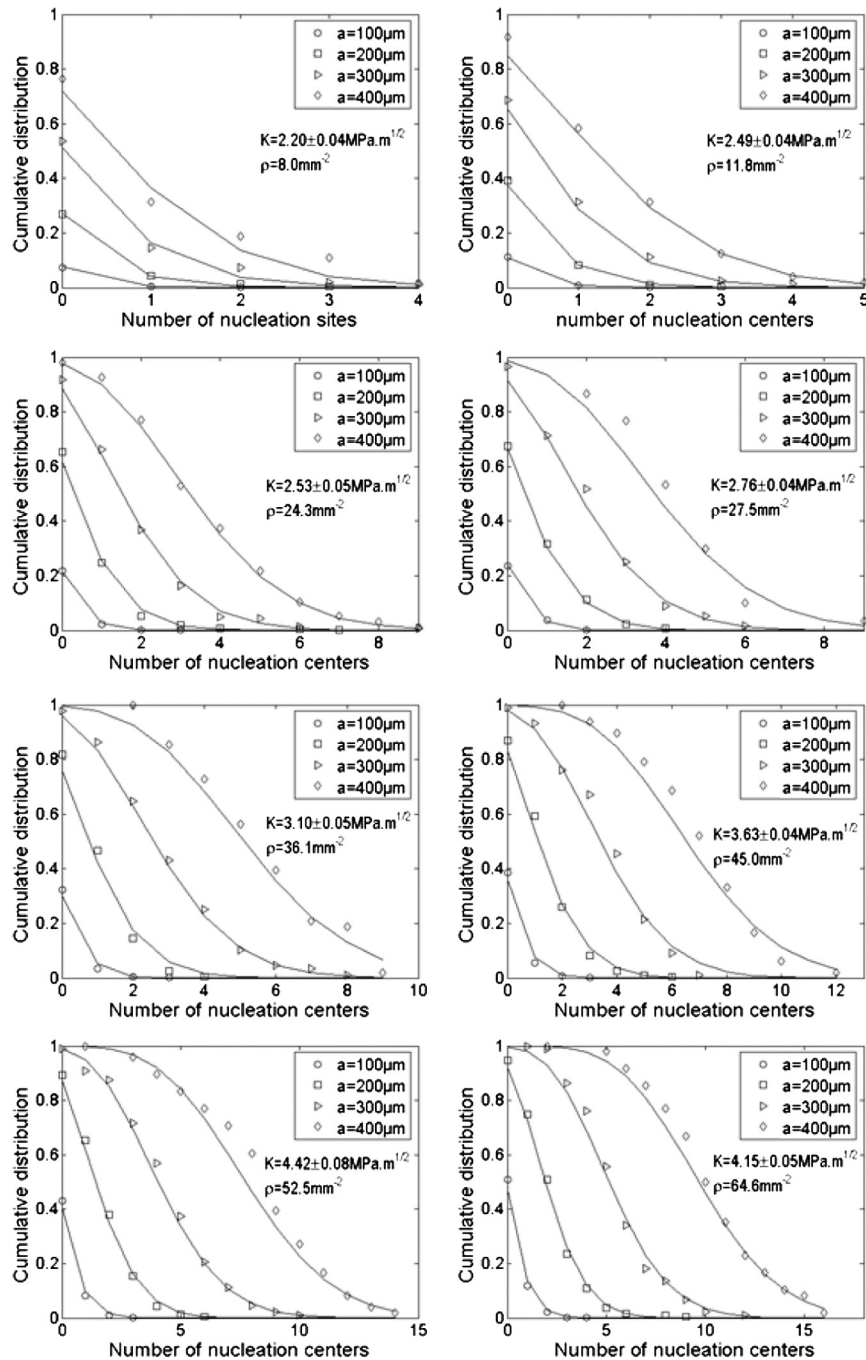
Fig. S3. Cumulative distribution of the number of nucleation centers contained in square regions of lateral size *a*, for each of the eight fractographic images analyzed. The cumulative distribution is defined as the proportion of square regions containing a number of nucleation centers which is strictly superior to the value in abscissa. Four values of *a* were chosen, namely *a* = 100, 200, 300, and 400 μm. In each graph, solid lines represent Poisson fits $P(n) = \sum_{k=0}^{n}(\rho a^2)^k/k!$, where the fitting parameter ρ is the same in all four curves and hence defines the surface density of centers in each image. Note that the same Poissonian distribution was assumed in ref. 1. The stress intensity factor *K* applying on the macroscopic crack front at these points was computed using finite element calculations (*Materials and Methods*). Its value together with the fitted value ρ is reported in each graph inset.

1. Ravi-Chandar K, Yang B (1997) On the role of microcracks in the dynamic fracture of brittle materials. *J Mech Phys Solids* 45:535–563.
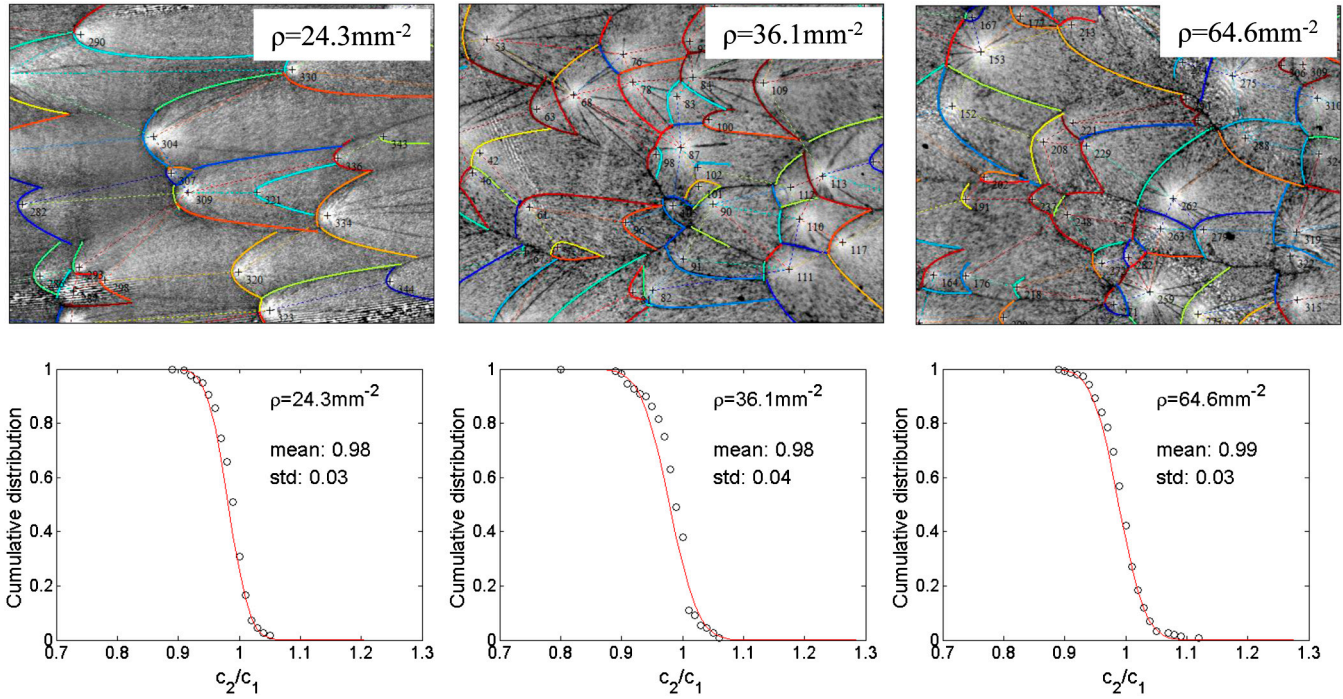
Fig. S4. Direct extraction of the relative speed between two interacting microcracks. (*Upper*) Typical examples of investigated zones (985×745 μm^2 in size) at three different microcrack densities. Each conic branch has been attributed a given color and the nuclei of the two corresponding interacting microcracks have been joined by a dotted segment of the same color. Note that a conic mark is often made of several of these branches. The ratio c_2/c_1 is the only adjustable parameter in Eq. **S1** to determine the branch geometry once the nuclei position and the branch apex are set. (*Lower*) Corresponding distributions for c_2/c_1. In the three cases, the distributions are found to fit normal distributions of mean value of approximately 0.98–0.99 and standard deviation of approximately 0.03–0.04, irrespective of ρ.
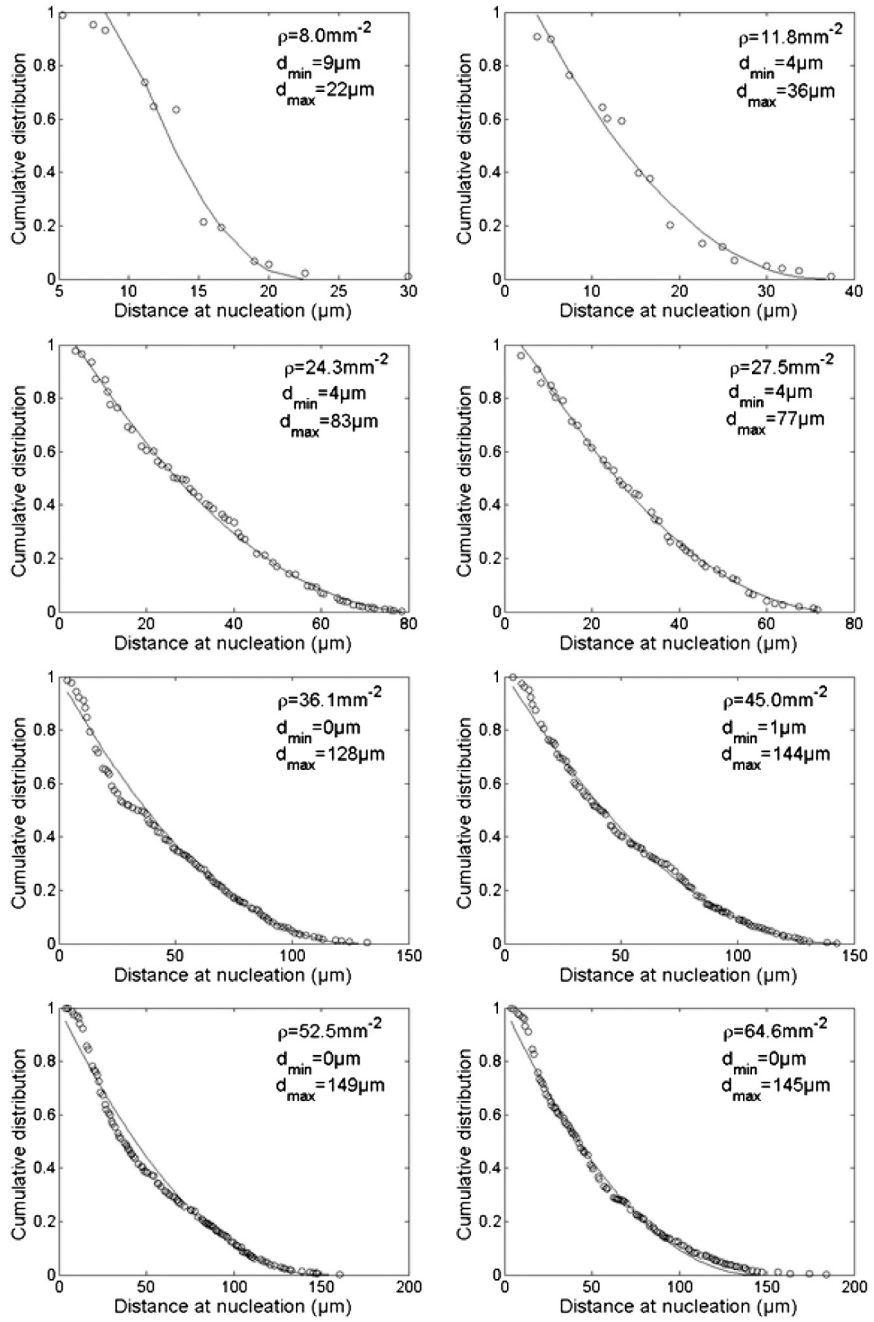
Fig. S5. Cumulative distribution, P, of the distance d_n between the triggering crack and the nucleation center at the time of nucleation, determined from each of the analyzed fractographic images. In each graph, the solid line shows the fit of the form $P(d_n) = [(d_{max} - d_n)/(d_{max} - d_{min})]^2$, where d_{min} and d_{max} are positive quantities. The fitted values d_{min} and d_{max} together with the surface density of nucleation centers ρ are reported in the inset in each graph. The value d_{min} decreases with ρ and becomes equal to zero when ρ is larger than 36 mm^{-2}. The value d_{max} increases with ρ over the whole explored range. Neglecting the small value of d_{min} allows us to use a single parameter [e.g., $\bar{d}_n(\rho)$] to define the whole distribution and its variations.
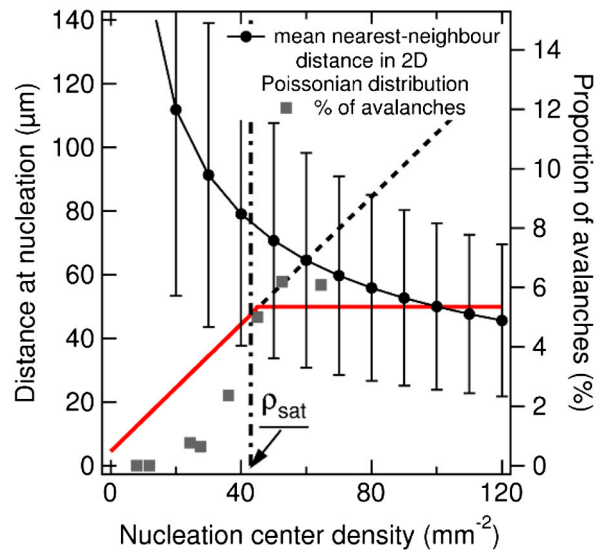
Fig. S6. Saturation of $\bar{d}_n$ and avalanches. Evolution of the fitted mean distance at nucleation, $\bar{d}_n$, (thick red line, see Fig. 3C, *Lower*), as a function of ρ. It is compared to the mean nearest-neighbor distance in a Poissonian distribution $1/(2\sqrt{\rho})$ (black solid line, error bars correspond to ±one standard deviation approximately $0.26/\sqrt{\rho}$). Solid squares indicate the proportion of microcracks involved in avalanches, as computed from the reconstruction.
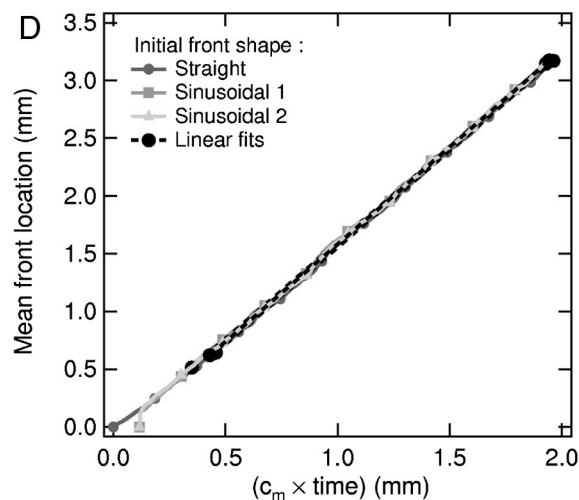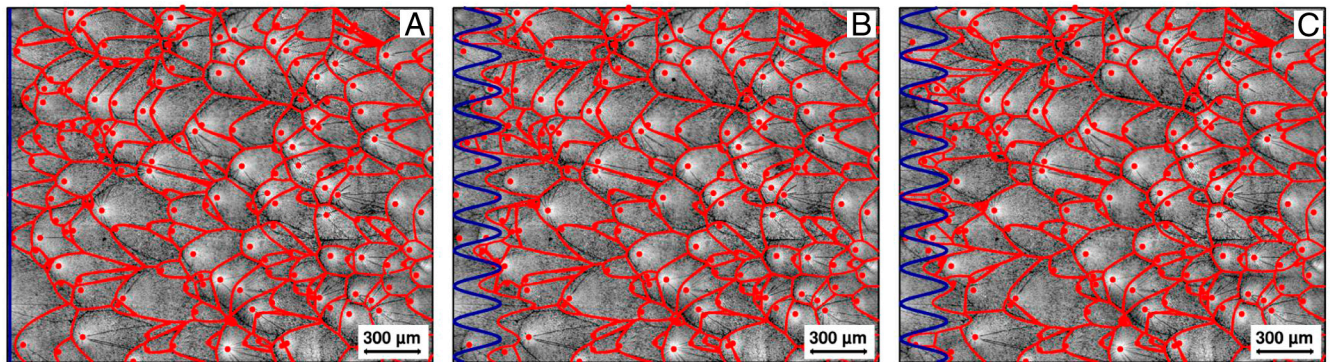

Fig. S7. Influence of edge effects on the reconstruction and average velocity. (*A–C*) Fracture surface images (gray level) compared to the reconstructed conic marks (red lines), for $\rho = 45.0$ mm^{-2} ($K \simeq 3.65$ MPa·m$^{1/2}$). Three different initial conditions were used. (*A*) Straight vertical line. (*B*) Vertical sinusoidal shape with a period of 186 μm and a peak-to-peak amplitude of 242 μm. (*C*) Same sinusoidal shape, but translated vertically over half a period. In all cases, red dots indicate nucleation centers. (*D*) Time evolution (scaled by c_m) of the average location of the simulated crack front for the three different initial front shapes. For each curve, the dashed line is a linear fit of the data between the two black dots. The fitted slopes between the black dots, which directly give the value of the acceleration factor A, are 1.679 ± 0.001 (straight), 1.666 ± 0.001 (sinus 1), and 1.687 ± 0.001 (sinus 2). These almost identical slopes show that the value of A is hardly sensitive to edge effects in the reconstruction.
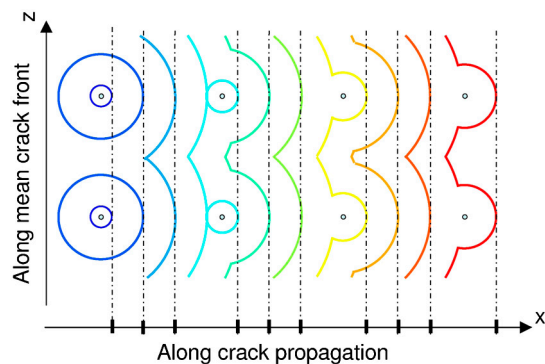
Fig. S8. Sketch of the mean-field model used to establish the relationship between the acceleration factor A, the microcrack density ρ, the mean distance at nucleation $\bar{d}_n$, and the microscopic velocity c_m of microcrack growth (Eq. **1** in the main text). The nucleation centers are placed on the nodes of a square lattice. The crack front is plotted at 10 successive times separated by a constant interval $\bar{d}_n/c_m$ (from blue to red). At each time, the rightmost point of the front is projected along the x axis (thick black ticks on the x axis). It propagates at a constant velocity c_m between coalescence events and jumps over a distance $\bar{d}_n$ at coalescence.
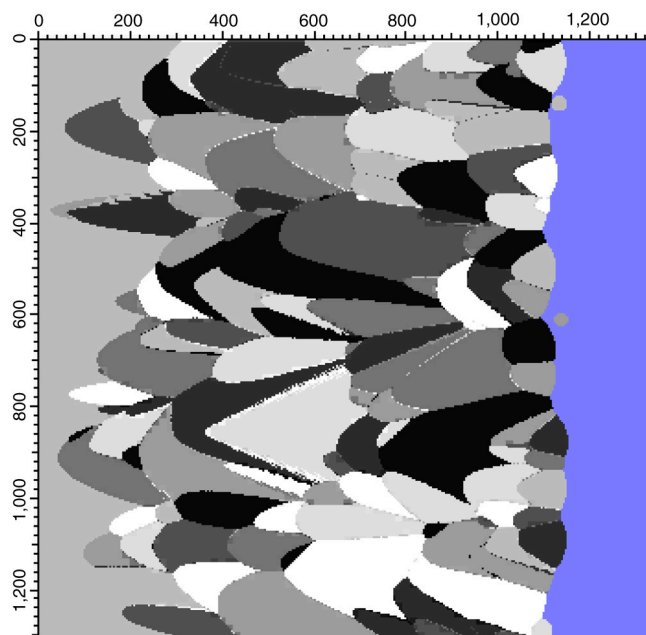
Movie S1. Movie of the reconstructed microscopic dynamics of crack propagation and microcracking events, for a density of microcracks $\rho = 27.5$ mm^{-2}. It shows a region of size $\simeq 2,500 \times 2,400$ μm during $\simeq 9.8$ μs.

Movie S1 (MOV)
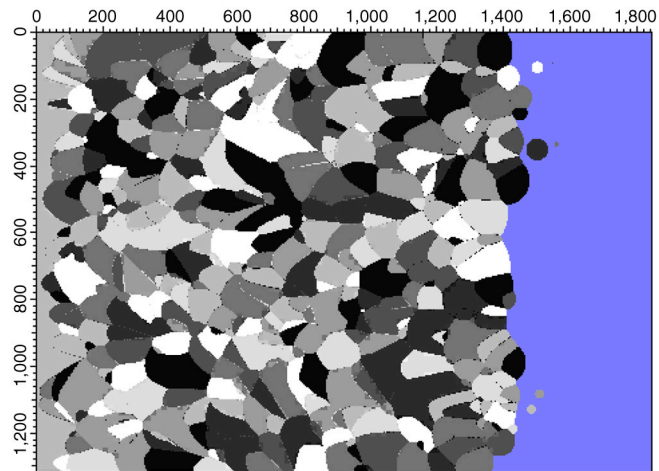
Movie S2. Movie of the reconstructed microscopic dynamics of crack propagation and microcracking events, for a density of microcracks $\rho = 64.6$ mm^{-2}. It shows a region of size $\simeq 3{,}400 \times 2{,}500$ μm during $\simeq 8.5$ μs.

Movie S2 (MOV)